

Article

MnO₂/AgNPs Composite as Flexible Electrode Material for Solid-State Hybrid Supercapacitor

Borislava Mladenova, Mariela Dimitrova and Antonia Stoyanova *

Institute of Electrochemistry and Energy Systems, Bulgarian Academy of Sciences, G. Bonchev Str. 10, 1113 Sofia, Bulgaria; borislava.mladenova@ees.bas.bg (B.M.); mariela.dimitrova@ees.bas.bg (M.D.)

* Correspondence: antonia.stoyanova@ees.bas.bg

Abstract: A MnO₂/AgNP nanocomposite was synthesized using a sonochemical method and investigated as an electrode material in a solid-state hybrid supercapacitor. Aquivion's sodium and lithium electrolyte membrane serves as an electrolyte and separator. For comparison, MnO₂ was used as the active material. The developed supercapacitor containing a carbon xerogel as a negative electrode, the MnO₂/AgNP composite as a positive electrode and a Na⁺-exchange membrane demonstrated the highest performance characteristics. These results indicate that the incorporation of silver nanoparticles into the MnO₂ structure is a prospect for obtaining an active composite electrode material for solid-state supercapacitors.

Keywords: MnO₂/AgNP nanocomposite; solid-state supercapacitor; Aquivion electrolyte membrane

1. Introduction

Supercapacitors (SCs) are energy storage devices that have extremely high power densities but do not reach the energy density of batteries and fuel cells. In recent years, research interest has focused on hybrid supercapacitors, which provide higher specific capacitance and improved energy density characteristics without changing the power density compared to existing electric double-layer capacitors (EDLCs) and pseudocapacitors [1]. There is also a growing interest in SCs with polymer electrolytes and flexible electrodes as they provide highly efficient and safe energy storage solutions for the rapidly developing application areas in consumer electronics and microelectronics [2].

Manganese oxide is a well-known electroactive material for SCs because of its low price, ideal capacitive behavior, theoretical specific capacity around 1370 F g⁻¹ and high cyclic stability (over 5000 cycles) [3–5]. However, conventional MnO_x-based supercapacitors suffer from limitations such as low electrical conductivity and insufficient interface surface area. To address these challenges, the hybridization of MnO_x with other highly conductive materials and increasing its porosity have emerged as promising approaches [6].

Ag stands out among the recently explored conductive materials because of its excellent conductivity and affordability. Lately, Ag nanoparticles (AgNPs) have found an application as conductive additives in energy storage systems. Recent research indicates that electrode materials doped with these elements can establish electron transport pathways owing to their superior electrical conductivity and notable surface activity. Consequently, the incorporation of Ag helps sustain the low internal resistance of metal oxide electrodes while enhancing proton diffusion across the electrodes. For example, RuO₂ doped with Ag shows a much higher specific capacitance than pure RuO₂. It has been found that the incorporation of silver nanoparticles into the structure of MnO₂ during discharge leads to the formation of similar channels and thus significantly improves the conductivity of the oxide and shows an increase in specific capacitance [7–10].

Silver-containing hybrid MnO_x nanostructures (silver–manganese oxide (Ag-MnO_x) and silver–manganese oxide with cetyltrimethylammonium bromide (c-Ag-MnO_x)) were synthesized and investigated as a positive electrode material in SCs [6]. Utilizing silver as



Citation: Mladenova, B.; Dimitrova, M.; Stoyanova, A. MnO₂/AgNPs Composite as Flexible Electrode Material for Solid-State Hybrid Supercapacitor. *Batteries* **2024**, *10*, 122. <https://doi.org/10.3390/batteries10040122>

Academic Editor: Xin Chen

Received: 1 March 2024

Revised: 1 April 2024

Accepted: 3 April 2024

Published: 5 April 2024



Copyright: © 2024 by the authors. Licensee MDPI, Basel, Switzerland. This article is an open access article distributed under the terms and conditions of the Creative Commons Attribution (CC BY) license (<https://creativecommons.org/licenses/by/4.0/>).

a conductive additive to MnO_x is motivated not only by its cost-effectiveness compared to other noble metals but also by its comparatively greater operational stability in comparison to transition metals and conducting polymers like polypyrrole [11,12]. Using gas-phase evaporation-induced self-assembly, silver nanoparticles are uniformly dispersed within the hybrid nanostructure, establishing a conductive pathway at the interface of the MnO_x crystallite cluster [6].

Despite the advantages shown, high SC values have not yet been achieved in Ag–metal oxide composites as there are problems related to their reduced surface area, ease of oxidation and tendency to agglomerate [13].

It should be noted that the optimization of any electrode material should always be carried out in combination with the electrolyte used, as the electrode and electrolyte should show good interaction and increased cycling stability. Polymer electrolyte and ion-exchange membranes can be effectively used as separators and electrolytes for the development of supercapacitor devices. The Aquion membrane exhibits superior proton conductivity and thermal stability in comparison to the Nafion membrane. This is attributed to its shorter side chain, higher glass transition temperature, increased crystallinity and lower equivalent weight. Additionally, the Aquion membrane demonstrates excellent chemical stability and is capable of operating at elevated temperatures, rendering it highly promising for utilization in energy systems [14]. The advantages of solid-state SCs, such as their light weight, small size, easy operation, excellent reliability and wider temperature range, are also significant factors for their development [15]. Neutral electrolytes are widely used in supercapacitor systems. Various factors such as the electrolyte pH, type of cations and anions, concentration of salts, different additives and solution temperature have been found to affect the device performance [16,17]. Their advantages, such as wider operating potential windows and increased protection, make them applicable in asymmetric and hybrid supercapacitors. Na_2SO_4 is the most widely used neutral electrolyte, promising for many pseudocapacitive materials (especially MnO_2 -based materials). Li (e.g., LiCl , Li_2SO_4 and LiClO_4), K (e.g., KCl , K_2SO_4 and KNO_3), Ca ($\text{Ca}(\text{NO}_3)_2$) and others are also common conducting salts in neutral electrolytes [18]. Alkali or alkaline earth metal cations, despite their similarities, exhibit variations in ionic sizes and hydrated ion sizes. These differences lead to distinct diffusion coefficients and ionic conductivity, consequently affecting the specific capacitance of the supercapacitor in diverse ways. For sulfate electrolytes of alkali metals, such as Li_2SO_4 , Na_2SO_4 and K_2SO_4 , some studies have shown that the values of the asymmetric specific capacitance of SCs follow the order $\text{Li}_2\text{SO}_4 < \text{Na}_2\text{SO}_4 < \text{K}_2\text{SO}_4$ [19–21]. MnO_2 stands as one of the most extensively investigated pseudocapacitive compounds in neutral electrolytes to date. Its charge–discharge cycle involves the alteration of Mn oxidation states from III to IV, accompanied by the surface adsorption–desorption or intercalation–deintercalation of electrolyte cations such as K^+ , Na^+ and Li^+ as well as protons (H^+). Given the direct involvement of electrolyte ions in the charge storage mechanism, the nature of neutral electrolytes is anticipated to exert a notable impact on the pseudocapacitive properties [18].

The aim of this research is to develop a new type of composite material containing MnO_2 and AgNPs to improve the performance of the positive electrode on solid-state supercapacitors and increase their energy density. The synthesized MnO_2 and MnO_2/AgNP samples were physicochemically characterized and electrochemically tested as flexible electrode materials in a hybrid supercapacitor cell. Na^+ and Li^+ forms of the commercial membrane Aquion® E87-05S (FullCellStore, Texas/USA) were used as the electrolyte and separator. The relationship between the nature of the electrolyte, the presence of AgNPs in the composite electrode material and the supercapacitor performance was investigated.

2. Materials and Methods

2.1. Synthesis of Materials

The MnO_2 and MnO_2/AgNP composite was synthesized in order to study its electrochemical behavior as an electrode material in supercapacitor cells. MnO_2 was obtained

by the ultrasound technique using manganese (II) chloride (Sigma-Aldrich, St. Louis, MO, USA) and potassium permanganate ($\geq 99.0\%$ Sigma-Aldrich) as reagents. These compounds were previously dissolved in distilled water and mixed, then the resulting suspension was treated for 1 h at room temperature in an ultrasonic bath (Siel, UST 5.7-150, Siel Ltd. Sofia, Sofia, Bulgaria). Precipitate formation was observed during synthesis.

To obtain the MnO_2/AgNP composite, AgNPs were initially synthesized by the chemical reduction of aqueous solution using ultrasonic field. The resulting nanoparticles were added to the suspension of MnCl_2 and KMnO_4 , during the synthesis of MnO_2 . A precipitate was formed which was washed repeatedly using a centrifuge (NEYA-16) at 5000 rpm, dried and subjected to further heat treatment at 200 °C to enhance the characteristics of the resulting material.

The carbon xerogel was prepared by the sol–gel methodology described in [22]. Here, resorcinol $\text{C}_6\text{H}_6\text{O}_2$ (Indspec, Petrolia, PA, USA, 99.6% purity) and formaldehyde CH_2O (Merck, Rahway, NJ, USA, 37% aqueous solution) were used as precursors. The pH of the precursor mixture was controlled, being 3 at the beginning of the process and increased to 6.5 using NaOH. This facilitates the polymerization reaction, and it is possible to have good control over the physicochemical properties of the resulting material.

2.2. The Preparation of the Electrodes and the Activation of the Polymer Electrolyte Membrane

The carbon electrodes were obtained by preparing an ink containing 80 wt.% xerogel, 10 wt.% ABG 1005 EG1 graphite and 10 wt.% polyvinylidene difluoride (PVDF) dissolved in 1-methyl-2-pyrrolidone [22]. The prepared ink was thoroughly mixed to ensure homogeneity before being coated onto a glass plate and subsequently dried at 70 °C for 12 h. Following this, each layer was meticulously removed from the glass plate and subjected to further drying at 120 °C for 1 h, followed by a final drying step at 160 °C for 20 min.

The synthesized MnO_2 and MnO_2/AgNP powders were used to fabricate a positive composite electrode. The ink consists of 75 wt% MnO_2 or MnO_2/AgNP , 10 wt% graphite ABG 1005 EG1, 5 wt% carbon fibers and 10 wt% PVDF binder in 1-Methyl-2-pyrrolidone solvent. Subsequently, the composite electrodes were manufactured in a process similar to that of carbon electrodes. The mass ratio between the carbon xerogel and composite electrodes is 1:1, the mass loading being 0.002 g.

A perfluorosulfonic acid (PFSA) membrane, specifically the Aquion® E87-05S model, supplied by Sigma-Aldrich in Italy, with a thickness of 50 μm and an equivalent weight of 870 g mol^{-1} , was used both as an electrolyte and as a separator. Prior to use, the polymer membrane was activated to Na^+ and Li^+ forms by immersion in solutions of 1 M Na_2SO_4 and 1 M $\text{Li}_2\text{SO}_4 \cdot \text{H}_2\text{O}$, respectively, for three hours at room temperature.

2.3. The Physicochemical Characterization of the Prepared Materials

The synthesized materials were analyzed using an X-ray powder diffractometer (XRD), in particular a PANalytical Aeris, operating with $\text{CuK}\alpha$ radiation ($\lambda = 1.5406\text{\AA}$) and $\theta\text{-}\theta$ using Bragg–Brentano geometry. The 2θ scanning range starts from 20 to 80° (scan step 0.02°, 60 s). The analysis of diffractograms was conducted utilizing the PDF-2 2022 database from the ICDD. The determination of the elemental composition was accomplished through energy-dispersive X-ray fluorescence spectrometry (EDXRF). The spectrometer Epsilon 1 (Panalytical, Malvern, UK) was employed to gather the spectra, equipped with a Ag target X-ray tube capable of operating at a voltage of 50 kV and a maximum power of 10 W. The elements that can be measured by this instrument unit range from sodium (Na) to americium (Am).

The sample morphology was examined using a scanning electron microscope, SEM (Zeiss Evo 10), following the careful application of a carbon coating to avoid surface charge accumulation. Energy-dispersive analysis (EDX) was conducted using the Zeiss Smart EDX system. Additionally, transmission electron microscope (TEM) analyses were performed using the JEOL JEM 2100, operating at 80–200 kV (Jeol Ltd. Akishima, Japan).

The porous texture of the obtained materials was investigated with a Quantachrome (Boynton Beach, FL, USA) AutoSorb iQ apparatus. The pore size distribution was determined using the BJH method. The obtained silver nanoparticles were analyzed using a scanning spectrophotometer (Shimadzu UV-1900i, Kyoto, Japan) in the range from 300 to 700 nm.

The measurement of the wetting angle consisted of dropping 10 μL of the electrolyte onto the electrode and observing the drop shape. Each determination was performed 5 times to obtain an average value for each sample using a KRÜSS K100 Force Tensiometer K100.

2.4. Electrochemical Characterization

The solid-state supercapacitors were electrochemically investigated to determine their performance. Cyclic galvanostatic charge–discharge (GCD) and long-term durability tests were performed using an Arbin BT-2000 instrumented system. Galvanostatic charge–discharge measurements were conducted from 0.05 to 1.6 V at a current load of 60, 90, 120, 240, 480, 600, 900 and 1200 mAg^{-1} , involving 30 cycles per step. Long-term cell tests were carried out at a current load of 240 mAg^{-1} for up to 1000 cycles. CV experiments were performed using the Multi PalmSens system (model 4, Houten, The Netherlands) at a constant voltage window and different scan rates of 1, 10, 20 and 40 mVs^{-1} . Electrochemical impedance spectroscopy (EIS) measurements were performed on the same setup, with frequency ranges from 10 MHz to 1 mHz.

The specific capacitance, energy density E and power density P of the developed supercapacitors were calculated using Equations (1)–(4) [23].

The specific capacitance C_s (Fg^{-1}) was determined based on cyclic voltammetric curves using the equation as follows:

$$C_s = [4(I/(dV/dt))/m], \quad (1)$$

where I is the current (A), dV/dt is the voltage scan rate (Vs^{-1}) and m is the mass of the active material (g).

The specific capacitance C (Fg^{-1}) derived from the galvanostatic charge–discharge tests was calculated from Equation (2):

$$C = [2(I \times \Delta t)/(m \times \Delta V)], \quad (2)$$

where I (A), Δt (s), m (g) and ΔV (V) are the discharge current, discharge time, mass of the active composite material and voltage window, respectively.

The energy density E (Whkg^{-1}) and the power density P (Wkg^{-1}) were calculated using Equations (3) and (4):

$$E = C \Delta V^2 / 7.2 \quad (3)$$

$$P = 3600 E / t \quad (4)$$

3. Results and Discussion

In Figure 1, the UV-Vis spectrum of a 5 mM AgNO_3 solution containing silver nanoparticles obtained by treatment in an ultrasonic bath at 50 °C is shown. The figure shows an absorption peak with a maximum at a wavelength around 413 nm, characteristic of spherical particles. The appearance of this peak in the spectrum is due to the Surface Plasmon Resonance (SPR) and is associated with the formation of silver particles of colloidal size. As a consequence of the successfully synthesized nanoparticles, we continued with their further integration into our materials.

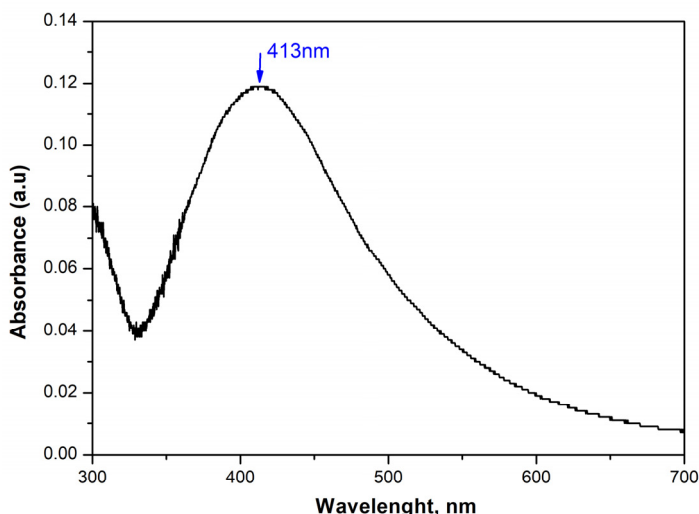


Figure 1. The UV-Vis spectrum of a solution synthesized in an ultrasonic field with 5 mM AgNO₃.

Figure 2 presents the X-ray diffraction (XRD) results of the obtained materials without being normalized. The appearance of broad peaks in the XRD patterns of both samples indicates the fine dispersity of the materials. The diffractogram of the synthesized MnO₂ shows a pronounced peak at 37.52° 2θ. The appearance of broader peaks with lower intensity at 25.71° and 66.69° 2θ corresponds to the (211), (220) and (112) planes characteristic of the α-MnO₂ structure. In the composite material MnO₂/AgNP, the increase in the intensity of the MnO₂ main peak can be associated with the presence of the introduced Ag nanoparticles and their partial oxidation as a result of the additional thermal treatment of the material at a temperature of about 200 °C. The main peak of MnO₂ overlaps with those of the cubic structure of Ag in the (111) direction at 37.71° 2θ, also of monoclinic AgO at 37.23 2θ. The availability of AgO was proven by the appearance of its main peak at 32.33° and others at 39.43 and 56.76 2θ, corresponding to the (−111), (−202) and (−113) crystallographic planes of the monoclinic structure of AgO.

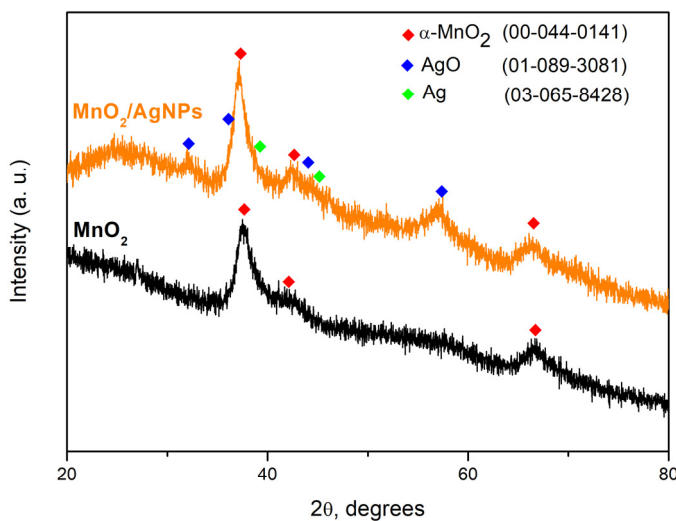


Figure 2. X-ray powder diffraction patterns of ultrasonically synthesized MnO₂ and MnO₂/AgNP and comparison with ICSD database.

The crystallite sizes (*t*) were calculated using Scherer's formula: $t = \kappa\lambda/B\cos\theta$ (5), where κ represents the shape factor (with a value of 0.9 for spherical crystals), λ (in Å) denotes the wavelength, θ is the diffraction angle of the peak and B (in radians) corresponds to the line broadening at the full width at half maximum (FWHM) values of the peaks.

The crystallite size at $37.5^\circ 2\theta$ (the primary orientation for the three crystallized phases) is roughly 5 nanometers, affirming the fine-grained characteristic of the materials.

Table 1 presents the results of the Rietveld analysis. It can be seen that structural modifications occur after the incorporation of AgNPs into the material. A change in the unit cell parameters of MnO_2 was observed, leading to a decrease in its volume.

Table 1. Unit cell parameters of synthesized MnO_2 and MnO_2/AgNP materials.

Sample	Phases	Quantity [wt %]	Unit Cell Parameters						t [nm]
			a [\AA]	b [\AA]	c [\AA]	α [$^\circ$]	β [$^\circ$]	γ [$^\circ$]	
MnO_2	MnO_2	100	9.9340	9.9340	2.8382	90	90	90	280.08
	MnO_2	93.51	9.8038	9.8038	2.8385	90	90	90	272.82
	AgO	4.04	6.0884	3.4175	5.4073	90	109.107	90	106.31
		2.45	4.0855	4.0855	4.0855	90	90	90	5.36

The qualitative and quantitative elemental analysis of the materials was determined by the XRF technique and was consistent with the XRD study. The quantitative analysis is shown in Table 2. The registration of K in the samples can be explained by the presence of unreacted potassium permanganate which, due to its low percentage content, was not registered as an available phase in the X-ray structural analysis.

Table 2. Qualitative and quantitative elemental analysis of synthesized nanocomposites.

Sample	Element (%)		
	Mn	Ag	K
MnO_2	96.54	---	3.46
MnO_2/AgNP	91.75	7.09	1.16

The pore size distribution of MnO_2/AgNP and MnO_2 is shown in Figure 3, and Table 3 presents the main characteristics and active surface area of both materials.

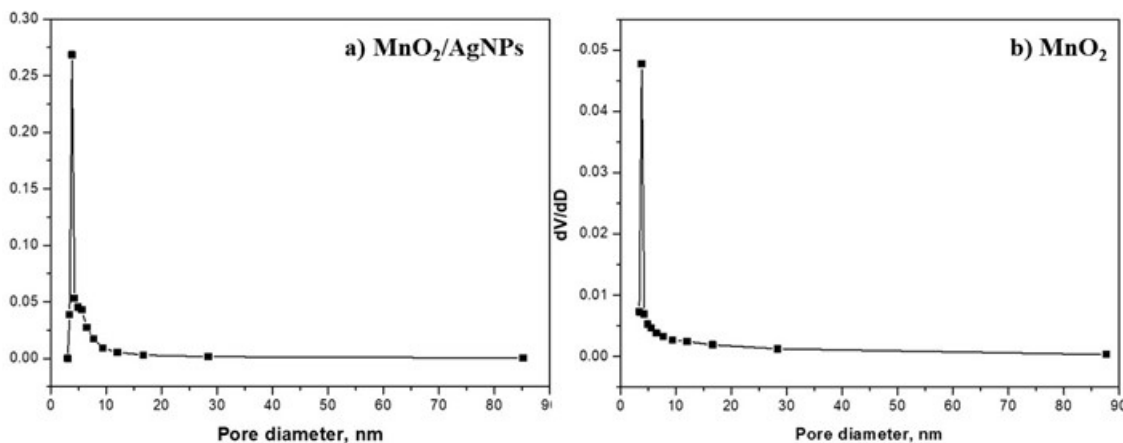


Figure 3. Pore size distribution for (a) MnO_2/AgNP and (b) MnO_2 .

Table 3. Main porous parameters for the MnO_2/AgNP and MnO_2 obtained from N_2 adsorption: specific surface area (SBET), total pore volume (V_t) and average pore diameter (nm).

Samples	SBET (Multi-Point BET), m^2g^{-1}	V_t , cm^3g^{-1}	D_{av} (4V/S), nm
MnO_2	47	0.124	11
MnO_2/AgNP	162	0.346	9

The active surface area of the composite material containing MnO_2 and AgNPs is $162.3 \text{ m}^2\text{g}^{-1}$, and it is about four times smaller at $46.6 \text{ m}^2\text{g}^{-1}$ for MnO_2 , which is a prerequisite for its better properties as an electrode material. The pore size distribution (Barrett–Joyner–Halenda, BJH) of the MnO_2/AgNP sample exhibited a sharp and narrow peak at 3.8 nm with a relatively narrow range from 3 to 17 nm. For the MnO_2 sample, the results were similar, with the main peak centered again at 3.8 nm and the pore size distribution ranging from 3.5 to 16.4 nm. The average pore size for the two materials was almost the same, 9 nm (for MnO_2/AgNP) and 11 nm (for MnO_2), and mesopores exist with the presence of macropores.

The SEM images of both samples (Figure 4) show multiple irregularly shaped particles as well as individual larger agglomerates. The particle size ranges from approximately 300 to 900 nm. In the MnO_2/AgNP composite, lighter particles (under 100 nm) were observed located on the MnO_2 surface (Figure 4, highlighted in red). It is assumed that these are AgNPs, in agreement with the results of UV-VIS and XRD analyses. The morphological observation confirms the conclusions already drawn regarding the nanostructural nature of the materials. EDX analysis also shows a clear high-intensity peak with energy corresponding to Ag in the MnO_2/AgNP sample, while this peak is absent in pure MnO_2 . The presence of K recorded in the spectra of both samples is related to the unreacted KMnO_4 , as previously discussed.

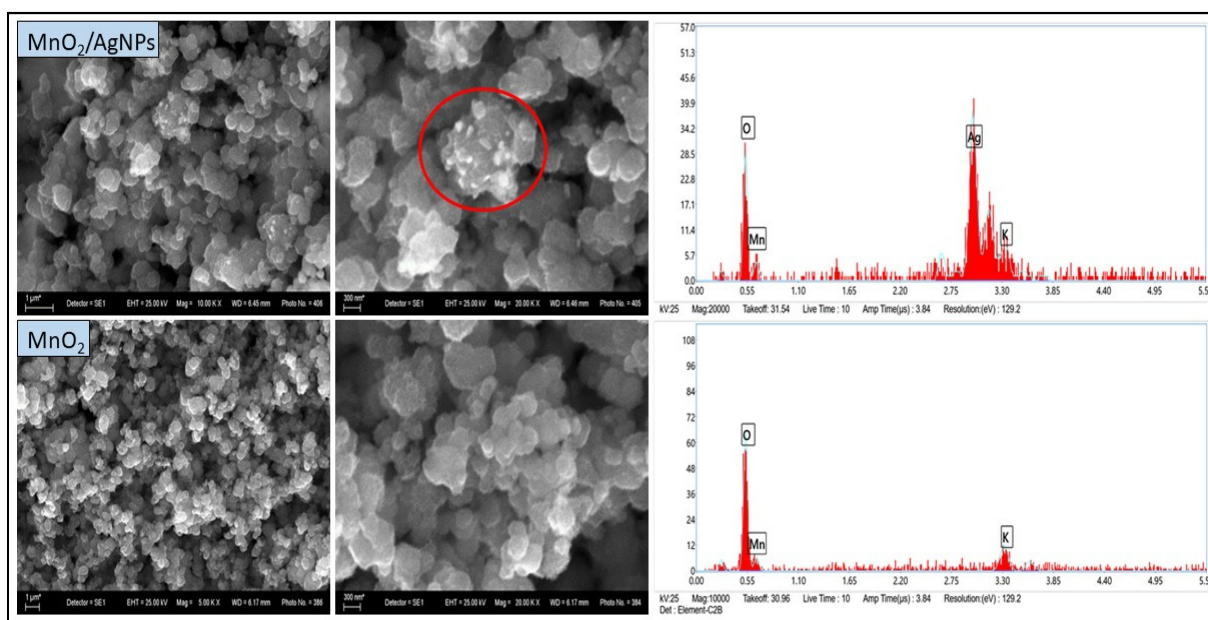


Figure 4. SEM images (left) and EDX spectra (right) of MnO_2 obtained by chemical reduction in aqueous medium.

The morphological characteristics of the synthesized materials (MnO_2 and MnO_2/AgNP) were further investigated with a transmission electron microscope, at a magnification of 40,000 times, and the results are presented in Figure 5. The TEM image of MnO_2 shows the formation of thread-like particles interconnected and thus forming a network. In the TEM image of the MnO_2/AgNP composite, the same network was observed, but in this case, it is denser due to the silver nanoparticles integrated into the manganese oxide structure. Single silver nanoparticles located on the periphery of the material with a size of about 20 nm are clearly visible, and in some places, the formation of individual clusters is also noticeable.

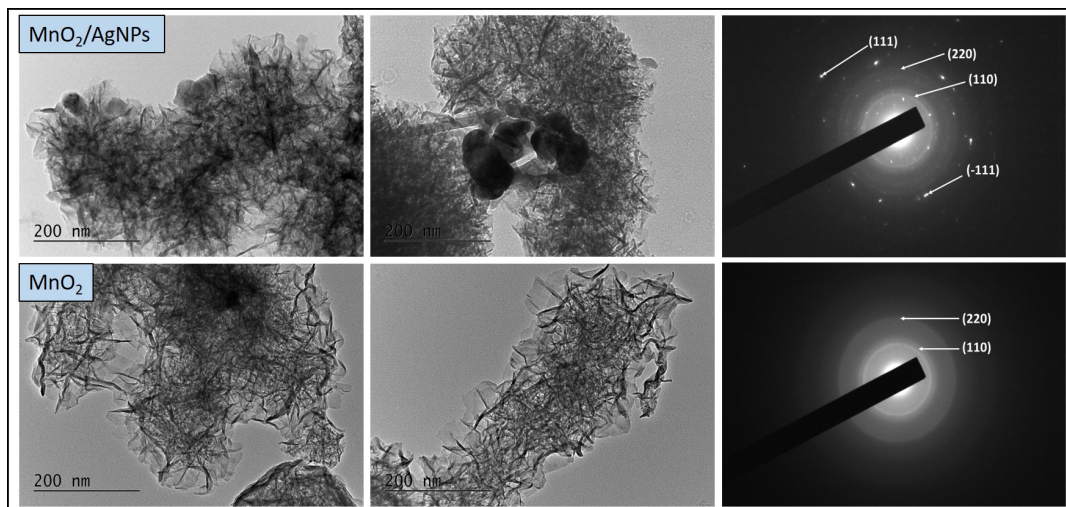


Figure 5. TEM images (left) and corresponding SAED patterns (right) of MnO_2/AgNP and MnO_2 .

The clearly defined concentric rings in the SAED images indicate the interplanar spacing in the crystal structure corresponding to the (110) and (220) orientations of $\alpha\text{-MnO}_2$. In the composite material, the appearance of additional rings was established, in accordance with the (111) direction of the face-centered cubic crystal lattice of silver nanoparticles, as well as (-111) of the monoclinic structure of silver oxide. These results fully confirm the XRD and SEM-EDX data.

The effect of the presence of Ag nanoparticles in the composite material on the performance of the supercapacitors was evaluated in two asymmetric configurations: $\text{AX}(-)/\text{/MnO}_2(+)$ and $\text{AX}(-)/\text{/MnO}_2/\text{AgNP}(+)$. The cells were electrochemically tested under identical experimental conditions using Na^+ - and Li^+ -exchange Aquion membranes as the electrolyte and separator (Figure 6).

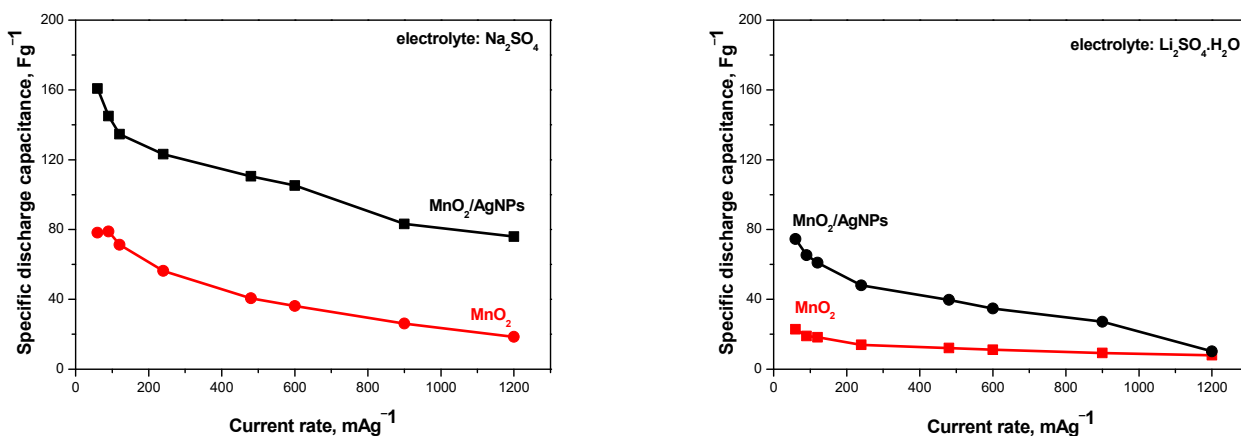


Figure 6. Discharge capacitance as a function of current rate for supercapacitors containing MnO_2 and MnO_2/AgNP electrodes and using Na^+ and Li^+ Aquion electrolyte membranes.

It can be seen that the supercapacitors containing the MnO_2/AgNP composite as the positive electrode show a higher discharge capacitance compared to SCs with MnO_2 in both electrolytes. The result obtained can be associated with the different pore structure and surface morphology of the two materials mentioned above, which determine their different capacitive behaviors. It is understood that the distribution of pore sizes can influence the accessibility of electrolyte ions to the electrode surface, thus influencing the system's capacitance [24]. MnO_2/AgNP has a much larger active surface area, which affects the diffusion of ions. As is known, the presence of mesopores in the material supports ion

diffusion to the macropores, thus transporting the ions from the electrolyte and forming an electric double layer [25]. It should also be kept in mind that the electrical conductivity of silver is very high, which is a prerequisite for Ag-doped metal oxides (in this case MnO_2) to exhibit high efficiency in the studied systems [13,26].

Figure 7 compares the cyclic voltammograms of MnO_2/AgNP in lithium- and sodium-based polymer electrolyte membranes. The voltammograms with the Na^+ -exchange membrane show a typical profile for supercapacitor systems with an almost rectangular shape. The curves overlap when the scan rate is increased from 1 to 40 mVs^{-1} , suggesting the excellent capacitive behavior of the devices [27]. For the Li^+ electrolyte, the rectangular shape of the CV profiles is not as well defined, and the curves at 1 mV/s differ significantly from those at higher rates. The oval profile of the CV curves using the Li^+ -exchange membrane as an electrolyte may be due to either slow electron transfer or slow/insufficient ion diffusion, i.e., limited charge–discharge kinetics [28].

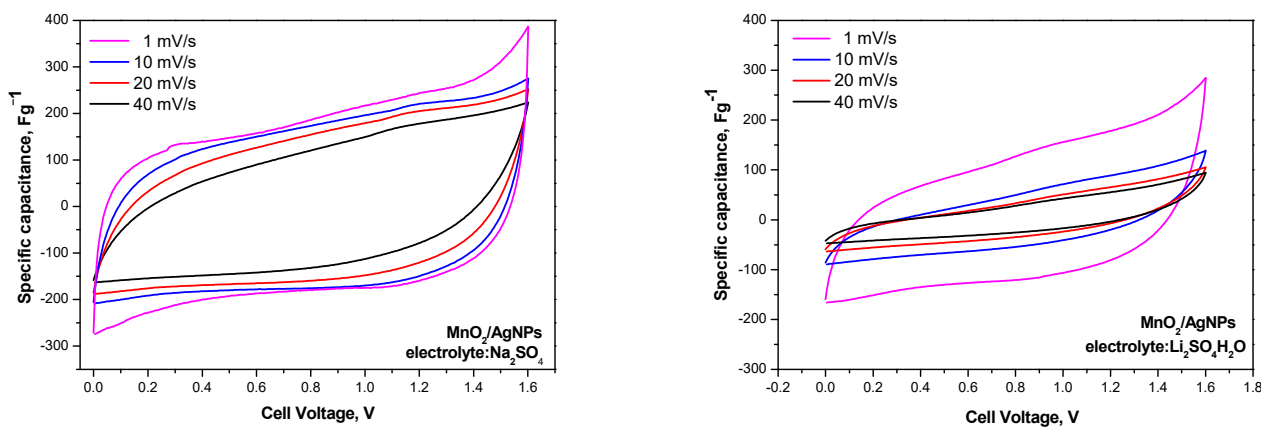


Figure 7. Cyclic voltammograms of asymmetric supercapacitors with MnO_2/AgNP electrodes and Na^+ and Li^+ Aquion membranes performed at scan rates ranging from 1 to 40 mVs^{-1} and a voltage window from 0.0 to 1.6 V.

The results of galvanostatic charge–discharge tests carried out at different current loads ($0.3\text{--}1.2 \text{ Ag}^{-1}$) of MnO_2/AgNP composite electrode supercapacitors in different electrolytes (respectively 1 M Na_2SO_4 and 1 M $\text{Li}_2\text{SO}_4\cdot\text{H}_2\text{O}$) are presented in Figure 8. It can be seen that the solid-state supercapacitor using the Na^+ -form Aquion membrane shows the highest and most stable specific discharge capacitance ($161 \text{ Fg}^{-1}\text{--}75 \text{ Fg}^{-1}$), followed by $\text{Li}_2\text{SO}_4\cdot\text{H}_2\text{O}$ ($75 \text{ Fg}^{-1}\text{--}10 \text{ Fg}^{-1}$). These data are consistent with the literature data showing that the neutral electrolyte is suitable for pseudocapacitive materials, especially those based on MnO_2 [29]. Furthermore, the capacitive characteristics are due to the different conductivity of the electrolyte and its interaction with the functional groups of the electrode material [30].

The different wettability of the electrode materials from the electrolyte is also a possible reason for the obtained result. It is well known that surface wettability effects affect the thermodynamic and dynamic properties of electrochemical energy storage systems [31] and can contribute to increasing the effective surface area, improving the specific capacitance and also the energy density of supercapacitors [32]. To this end, in the present study, the wetting angle of MnO_2/AgNP electrodes versus Na_2SO_4 and Li_2SO_4 electrolytes was measured (Figure 9).

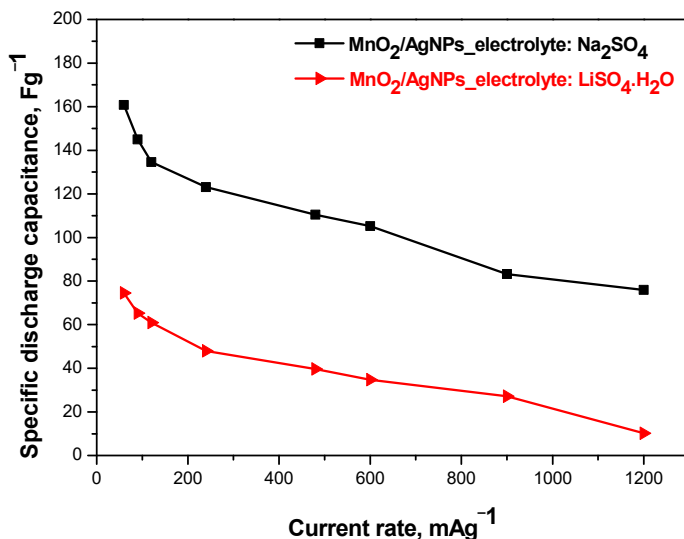


Figure 8. Comparison: discharge capacitance as function of current rate of MnO_2/AgNP SC with different electrolytes.

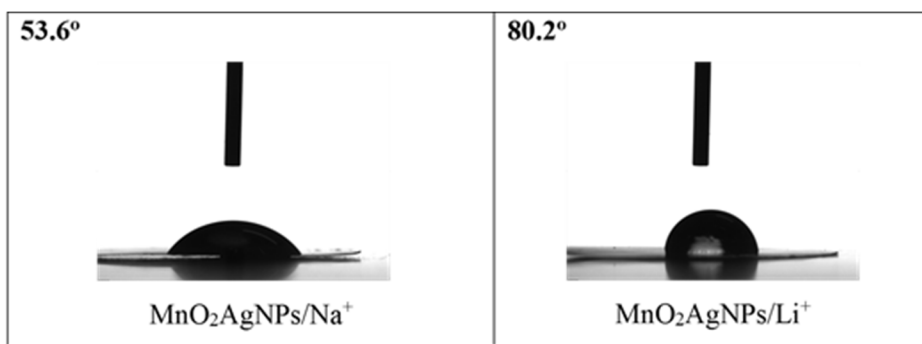


Figure 9. Wetting angles of MnO_2/AgNP electrode versus 1 M Na_2SO_4 and 1 M Li_2SO_4 .

The results show that the composite electrode shows better wettability with Na_2SO_4 than with Li_2SO_4 (the wetting angle is almost two times lower). Furthermore, in our previous work, it was shown that the Aquion membrane exhibits lower wettability, with no difference in response to the two electrolytes [22]. This may be largely related to their further electrochemical behaviors in the cell.

The good supercapacitive properties of hybrid devices with a $\text{MnO}_2/\text{AgNPs}$ positive electrode and Na^+ electrolyte can be seen from the Ragone plot. The comparative curves of cells using the Li^+ -exchange Aquion membrane show lower energy values compared to Na^+ (Figure 10).

The features of composite MnO_2/AgNP electrodes with Na^+ -form Aquion membranes were additionally investigated focusing on their cycling stability. Long-term testing covered 1000 charge and discharge cycles under a current load of 240 mA^{-1} (Figure 11).

From the long-term cycling, it is seen that SCs in Na_2SO_4 and $\text{Li}_2\text{SO}_4 \cdot \text{H}_2\text{O}$ have a 16 and 25% capacitance loss, respectively, with pronounced fluctuations in $\text{Li}_2\text{SO}_4 \cdot \text{H}_2\text{O}$. This probably indicates that the performance of the supercapacitor is affected by factors other than the ionic conductivity of the electrolyte and the ionic sizes of Li^+ and Na^+ [33]. The GCD curves at a discharge current rate of 240 mA^{-1} for SCs with a Na^+ -form membrane (Figure 10) show a typical shape for the behavior of a hybrid supercapacitor [34]. The iR drop is very low (0.083 V) and negligible considering the solid-state configuration of the cell [35].

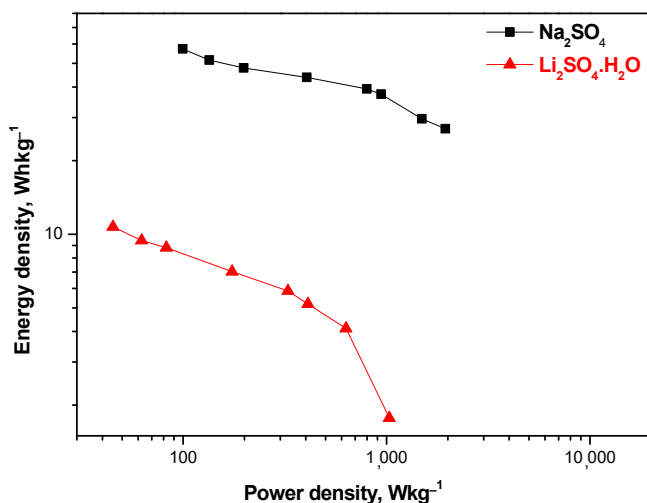


Figure 10. Energy density versus power density (Ragone plot) for SCs with MnO_2/AgNP and Na^+ - and Li^+ -exchange Aquion membrane.

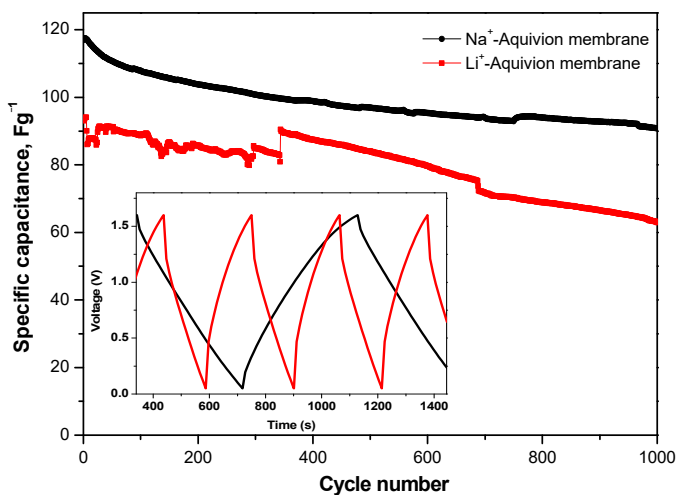


Figure 11. Long-term GCD tests at 240 mA g^{-1} for supercapacitors with MnO_2/AgNP using Na^+ - and Li^+ -form of Aquion electrolyte membrane. Inset figure—charge–discharge profile.

The EIS measurement of the cell with MnO_2/AgNP using the Na^+ form of the Aquion electrolyte membrane was conducted additionally. The Nyquist plot (Figure 12) is typical for an electrochemical supercapacitor. The inset figure represents the zoomed high-frequency region. The hinted depressed semicircle at high frequencies is a superposition of the semicircles due to the pore resistance R_p and charge transfer resistance R_{ct} of the two electrodes with a total value of 0.45Ω . The high frequency (left) intersection of the semicircle with the Z' axis gives the value of the series resistance ($R_s = 2 \Omega$) and is usually due to the resistance of the electrolyte as well as the electrical contacts. In the middle and low frequencies, the Nyquist diagram appears as straight lines with low ($<45^\circ$) and high ($>80^\circ$) slopes that describe the diffusion process and capacitive behavior, respectively. The intersection of the continuation of the capacitive line with the abscissa gives the internal resistance of the supercapacitor $R_{int} = R_s + R_p + R_{ct} + R_D = 3.9$ ohms (R_D is the diffusion resistance). This resistance is comparable to that of symmetrical carbon supercapacitors.

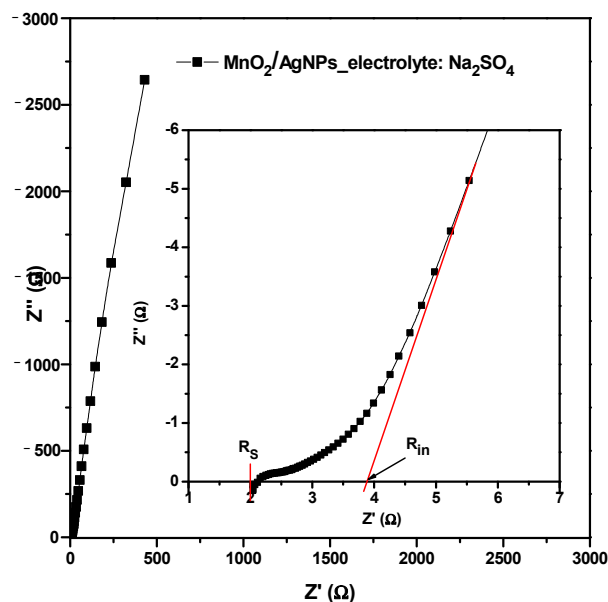


Figure 12. Nyquist plot for supercapacitor with MnO_2/AgNP using Na^+ form of Aquion electrolyte membrane. Inset figure is zoomed high-frequency region.

The shapes of the CV curves (Figure 7) show that both the Faraday reaction and the electric double layer contribute to the charge storage. Together with the Nyquist plots (Figure 12), this suggests an ideal capacitive behavior due to the fact that Ag nanoparticles can reduce the charge transfer resistance and improve electron transfer [36].

4. Conclusions

The MnO_2/AgNP composite material was successfully synthesized and characterized structurally and morphologically using various analyses. The resulting material has a four-times-higher active surface area ($162 \text{ m}^2 \text{ g}^{-1}$) than that of MnO_2 synthesized and investigated as a reference material. Electrochemical tests were carried out with the Na^+ and Li^+ form of the commercial membrane Aquion® E87-05S used as an electrolyte. The results show that MnO_2/AgNP is a suitable flexible electrode material for solid-state supercapacitors. The introduction of AgNPs into the manganese oxide nanostructure increases cell capacitance. The highest performance is achieved when a Na^+ -exchange membrane is used as the electrolyte (supercapacitors provide sufficiently high specific capacitances of $110\text{--}115 \text{ F g}^{-1}$ at 0.2 A g^{-1} , along with an energy density of 45 Wh kg^{-1} at 405 W kg^{-1} and in a voltage window of $0\text{--}1.6 \text{ V}$).

Author Contributions: Conceptualization, A.S., methodology, A.S. and B.M.; validation, B.M. and M.D.; investigation, B.M.; data curation, B.M. and M.D.; writing—original draft preparation, B.M.; writing—review and editing, A.S.; visualization, B.M.; project administration, B.M.; funding acquisition, B.M. All authors have read and agreed to the published version of the manuscript.

Funding: This research was funded by the Bulgarian Ministry of Education and Science under the National Program “Young Scientists and Postdoctoral Students-2”.

Data Availability Statement: Data is contained within the article.

Acknowledgments: The authors gratefully acknowledge the support of the Bulgarian Ministry of Education and Science under the National Program “Young Scientists and Postdoctoral Students-2”. The authors thank Ana Arenillas for the carbon xerogel provided.

Conflicts of Interest: The authors declare no conflicts of interest. The funders had no role in the design of the study; in the collection, analyses, or interpretation of the data; in the writing of the manuscript; or in the decision to publish the results.

References

- Muzaffar, A.; Ahamed, M.B.; Deshmukh, K.; Thirumalai, J. A review on recent advances in hybrid supercapacitors: Design, fabrication and applications. *Renew. Sustain. Energy Rev.* **2018**, *101*, 123–145. [[CrossRef](#)]
- Gao, H.; Lian, K. Proton-Conducting Polymer Electrolytes and Their Applications in Solid Supercapacitors: A Review. *RSC Adv.* **2014**, *4*, 33091–33113. [[CrossRef](#)]
- Huang, M.; Li, F.; Dong, F.; Zhang, Y.X.; Zhang, L.L. MnO₂-based nanostructures for high-performance supercapacitors. *J. Mater. Chem. A* **2015**, *3*, 21380–21423. [[CrossRef](#)]
- Obeidat, A.M. Solid-state supercapacitors based on poly (3,4-ethylendioxythiophene) (PEDOT)—Manganese oxide (MnO₂) composite electrodes synthesized by single-step Co-Deposition for electrical energy storage. *Mater. Today Energy* **2018**, *10*, 81–88. [[CrossRef](#)]
- Li, C.; Dong, X.; Zhang, Y.; Hu, J.; Liu, W.; Cui, X.; Hao, A. MnOx nanosheets anchored on a bio-derived porous carbon framework for high-performance asymmetric supercapacitors. *Appl. Surf. Sci.* **2020**, *527*, 146842. [[CrossRef](#)]
- Sun, Y.-A.; Chen, L.-T.; Hsu, S.-Y.; Hu, C.-C.; Tsai, D.-H. Silver Nanoparticles-Decorating Manganese Oxide Hybrid Nanostructures for Supercapacitor Applications. *Langmuir* **2019**, *35*, 14203–14212. [[CrossRef](#)] [[PubMed](#)]
- Xia, H.; Hong, C.; Shi, X.; Li, B.; Yuan, G.; Yao, Q.; Xie, J. Hierarchical hetero structures of Ag nanoparticles decorated MnO₂ nanowires as promising electrodes for supercapacitors. *J. Mater. Chem. A* **2014**, *3*, 1216–1221. [[CrossRef](#)]
- Yuksel, R.; Coskun, S.; Unalan, H.E. Coaxial silver nanowire network core molybdenum oxide shell supercapacitor electrodes. *Electrochimica Acta* **2016**, *193*, 39–44. [[CrossRef](#)]
- Nagamuthu, S.; Vijayakumar, S.; Muralidharan, G. Ag incorporated Mn₃O₄/AC nanocomposites based supercapacitor devices with high energy density and power density. *Dalton Trans.* **2014**, *43*, 17528–17538. [[CrossRef](#)]
- Ma, L.; Shen, X.; Ji, Z.; Zhu, G.; Zhou, H. Ag nanoparticles decorated MnO₂/reduced graphene oxide as advanced electrode materials for supercapacitors. *Chem. Eng. J.* **2014**, *252*, 95–103. [[CrossRef](#)]
- Chang, W.-C.; Tai, J.-T.; Wang, H.-F.; Ho, R.-M.; Hsiao, T.-C.; Tsai, D.-H. Surface PEGylation of silver nanoparticles: Kinetics of simultaneous surface dissolution and molecular desorption. *Langmuir* **2016**, *32*, 9807–9815. [[CrossRef](#)] [[PubMed](#)]
- Yang, J.; Lan, T.; Liu, J.; Song, Y.; Wei, M. Supercapacitor electrode of hollow spherical V₂O₅ with a high pseudocapacitance in aqueous solution. *Electrochimica Acta* **2013**, *105*, 489–495. [[CrossRef](#)]
- Guan, Y.; Guo, Z.; Che, H.; Mu, J.; Zhang, X.; Zhang, Z.; Wang, G.; Bai, Y.; Xie, H. Core/shell nanorods of MnO₂/carbon embedded with Ag nanoparticles as high-performance electrode materials for supercapacitors. *Chem. Eng. J.* **2018**, *331*, 23–30. [[CrossRef](#)]
- Aricò, A.S.; Di Blasi, A.; Brunaccini, G.; Sergi, F.; Dispenza, G.; Andaloro, L.; Ferraro, M.; Antonucci, V.; Asher, P.; Buche, S.; et al. High temperature operation of a solid polymer electrolyte fuel cell stack based on a new ionomer membrane. *Fuel Cells* **2010**, *10*, 1013–1023. [[CrossRef](#)]
- Lu, X.; Yu, M.; Wang, G.; Tong, Y.; Li, Y. Flexible solid-state supercapacitors: Design, fabrication and applications. *Energy Environ. Sci.* **2014**, *7*, 2160–2181. [[CrossRef](#)]
- Xu, C.; Wei, C.; Li, B.; Kang, F.; Guan, Z. Charge storage mechanism of manganese dioxide for capacitor application: Effect of the mild electrolytes containing alkaline and alkaline-earth metal cations. *J. Power Sources* **2011**, *196*, 7854–7859. [[CrossRef](#)]
- Wen, S.; Lee, J.-W.; Yeo, I.-H.; Park, J.; Mho, S.-I. The role of cations of the electrolyte for the pseudocapacitive behavior of metal oxide electrodes, MnO₂ and RuO₂. *Electrochimica Acta* **2004**, *50*, 849–855. [[CrossRef](#)]
- Sajjad, M.; Khan, M.I.; Cheng, F.; Lu, W. A review on selection criteria of aqueous electrolytes performance evaluation for advanced asymmetric supercapacitors. *J. Energy Storage* **2021**, *40*, 102729. [[CrossRef](#)]
- Fic, K.; Lota, G.; Meller, M.; Frackowiak, E. Novel insight into neutral medium as electrolyte for high-voltage supercapacitors. *Energy Environ. Sci.* **2011**, *5*, 5842–5850. [[CrossRef](#)]
- Qu, Q.; Wang, B.; Yang, L.; Shi, Y.; Tian, S.; Wu, Y. Study on electrochemical performance of activated carbon in aqueous Li₂SO₄, Na₂SO₄ and K₂SO₄ electrolytes. *Electrochim. Commun.* **2008**, *10*, 1652–1655. [[CrossRef](#)]
- Shao, J.; Li, X.; Qu, Q.; Wu, Y. Study on different power and cycling performance of crystalline K_xMnO₂·nH₂O as cathode material for supercapacitors in Li₂SO₄, Na₂SO₄, and K₂SO₄ aqueous electrolytes. *J. Power Sources* **2013**, *223*, 56–61. [[CrossRef](#)]
- Karamanova, B.; Mladenova, E.; Thomas, M.; Rey-Raab, N.; Arenillas, A.; Lufrano, F.; Stoyanova, A. Electrochemical Performance of Symmetric Solid-State Supercapacitors Based on Carbon Xerogel Electrodes and Solid Polymer Electrolytes. *Gels* **2023**, *9*, 983. [[CrossRef](#)] [[PubMed](#)]
- Sosarov, L.; Mladenova, B.; Karamanova, B.; Lefterova, E.; Arenillas, A.; Stoyanova, A. Comparative study of electrochemical performance of symmetric supercapacitors between aqueous electrolyte and polymer exchange membrane. *Monatshefte für Chem. Chem. Mon.* **2024**. [[CrossRef](#)]
- Yan, R.; Antonietti, M.; Oschatz, M. Toward the Experimental Understanding of the Energy Storage Mechanism and Ion Dynamics in Ionic Liquid Based Supercapacitors. *Adv. Energy Mater.* **2018**, *8*, 1800026. [[CrossRef](#)]
- Supiyeva, Z.; Pan, X.; Abbas, Q. The critical role of nanostructured carbon pores in supercapacitors. *Curr. Opin. Electrochem.* **2023**, *39*, 101249. [[CrossRef](#)]
- Karami, Z.; Youssefi, M.; Raeissi, K.; Zhiani, M. Effect of the morphology of silver layer on electrical conductivity and electrochemical performance of silver/reduced graphene oxide/cotton fabric composite as a flexible supercapacitor electrode. *J. Energy Storage* **2021**, *42*, 103042. [[CrossRef](#)]

27. Rey-Raab, N.; Menéndez, J.A.; Arenillas, A. RF xerogels with tailored porosity over the entire nanoscale. *Microporous Mesoporous Mater.* **2014**, *195*, 266–275. [[CrossRef](#)]
28. Huang, C.; Zhang, J.; Young, N.P.; Snaith, H.J.; Grant, P.S. Solid-state supercapacitors with rationally designed heterogeneous electrodes fabricated by large area spray processing for wearable energy storage applications. *Sci. Rep.* **2016**, *6*, 25684. [[CrossRef](#)] [[PubMed](#)]
29. Rodriguez-Romero, J.; de Larramendi, I.R.; Goikolea, E. Nanostructured Manganese Dioxide for Hybrid Supercapacitor Electrodes. *Batteries* **2022**, *8*, 263. [[CrossRef](#)]
30. Sahoo, M.K.; Rao, G.R. A high energy flexible symmetric supercapacitor fabricated using N-doped activated carbon derived from palm flowers. *Nanoscale Adv.* **2021**, *3*, 5417–5429. [[CrossRef](#)]
31. Zhao, S.; Song, Z.; Qing, L.; Zhou, J.; Qiao, C. Surface Wettability Effect on Energy Density and Power Density of Supercapacitors. *J. Phys. Chem. C* **2022**, *126*, 9248–9256. [[CrossRef](#)]
32. Liu, T.; Wang, K.; Chen, Y.; Zhao, S.; Han, Y. Dominant role of wettability in improving the specific capacitance. *Green Energy Environ.* **2019**, *4*, 171–179. [[CrossRef](#)]
33. Li, W.; Lu, H.; Zhang, N.; Ma, M. Enhancing the Properties of Conductive Polymer Hydrogels by Freeze–Thaw Cycles for High-Performance Flexible Supercapacitors. *ACS Appl. Mater. Interfaces* **2017**, *9*, 20142–20149. [[CrossRef](#)] [[PubMed](#)]
34. Guo, J.; Zhao, Y.; Jiang, N.; Liu, A.; Gao, L.; Li, Y.; Wang, H.; Ma, T. In-situ grown Ni(OH)₂ nanosheets on Ni foam for hybrid supercapacitors with high electrochemical performance. *J. Electrochem. Soc.* **2018**, *165*, A882–A890. [[CrossRef](#)]
35. Thomas, M.; Veleva, S.; Karamanova, B.; Brigandì, A.; Rey-Raab, N.; Arenillas, A.; Stoyanova, A.; Lufrano, F. Highly stable and reliable asymmetric solid-state supercapacitors with low self-discharge rates. *Sustain. Mater. Technol.* **2023**, *38*, e00770. [[CrossRef](#)]
36. Li, Z.; Wang, X.; Yin, Z.; Zhao, J.; Song, M.; Wu, Z.; Li, H.; Wang, X. Ag nanoparticles decorated N/S dual-doped graphene nanohybrids for high-performance asymmetric supercapacitors. *Carbon* **2020**, *161*, 726–735. [[CrossRef](#)]

Disclaimer/Publisher's Note: The statements, opinions and data contained in all publications are solely those of the individual author(s) and contributor(s) and not of MDPI and/or the editor(s). MDPI and/or the editor(s) disclaim responsibility for any injury to people or property resulting from any ideas, methods, instructions or products referred to in the content.